Interpreting atomic-resolution spectroscopic images

M. P. Oxley,[1] M. Varela,[1] T. J. Pennycook,[1] K. van Benthem,[1] S. D. Findlay,[2] A. J. D'Alfonso,[2] L. J. Allen,[2] and S. J. Pennycook[1]

[1]*Materials Science and Technology Division, Oak Ridge National Laboratory, P.O. Box 2008, Oak Ridge, Tennessee 37831, USA*

[2]*School of Physics, University of Melbourne, Victoria 3010, Australia*

(Received 19 March 2007; revised manuscript received 23 May 2007; published 8 August 2007)

Core-loss electron energy loss spectroscopy is a powerful experimental tool with the potential to provide atomic-resolution information about electronic structure at defects and interfaces in materials and nanostructures. Interpretation, however, is nonintuitive. Comparison of experimental and simulated compositional maps in $LaMnO_3$ shows good agreement, apart from an overall scaling of image contrast, and shows that the shape and width of spectroscopic images do not show a simple variation with binding energy, as commonly assumed, or with the size of the orbital excited. For the low lying La $N_{4,5}$ edge with threshold at around 99 eV, delocalization does not preclude atomic resolution, but reduces the image contrast. The image width remains comparable to that of the much higher lying O K edge with threshold at around 532 eV. Both edges show a volcanolike feature, a dip at the column position not previously seen experimentally. In the case of the O K edge, this represents an experimental verification of nonlocal inelastic scattering effects in electron energy loss spectroscopy imaging. In the case of the $N_{4,5}$ edge, the volcanolike feature is due to dynamical channeling and absorption of the probe through the specimen thickness. Simulation is therefore critical to the interpretation of atomic-resolution elemental maps.

DOI: 10.1103/PhysRevB.76.064303 PACS number(s): 42.30.Va, 61.14.Dc

I. INTRODUCTION

In the 13 years since the first demonstration of atomic-resolution electron energy loss spectroscopy (EELS) in the scanning transmission electron microscope (STEM),[1–3] it has been widely used in probing interfacial structure and bonding. Now, the ability to correct geometric aberrations has led to probe sizes of typically 1 Å or less.[4,5] This enables EELS measurements at unprecedented spatial resolution and the first definitive test of imaging theory at atomic resolution. A rigorous understanding of core-loss EELS image formation in the STEM requires not only a detailed description of the ionization process[6,7] but also an accurate description of the propagation of the incident probe through the crystal.[8,9] Interpretation of STEM images based on core-loss EELS is further complicated by the effective nonlocal interaction potential.[10] In this paper, we show experimental atomic-resolution core-loss images that confirm theoretical predictions and show the need for a full nonlocal treatment. Analysis of the thickness dependence of simulated images enables effects due to the nonlocal nature of the scattering potential to be distinguished from those due to dynamical propagation and absorption of the probe with increasing thickness. These results show that the maximum core-loss intensity cannot always be used to locate the corresponding atomic columns.

II. THEORY

The EELS image for a crystal of thickness t may be calculated as a function of probe position $\mathbf{R}$ using a synthesis of the mixed dynamic form factor formalism and the frozen phonon method[6–9,11] via the inelastic cross section expression:

$$\sigma(\mathbf{R},t) = \frac{1}{N}\sum_{n=1}^{N}\int_0^t \left[\sum_{\mathbf{h},\mathbf{g}} \mu_{\mathbf{h},\mathbf{g}} \Psi_n^*(\mathbf{R},\mathbf{h},z)\Psi_n(\mathbf{R},\mathbf{g},z)\right] dz. \quad (1)$$

Here, N is the number of different frozen phonon configurations used. We use an Einstein model to generate the frozen phonon configurations, an adequate approximation for these purposes.[12] The inelastic scattering coefficients for inner-shell ionization $\mu_{\mathbf{h},\mathbf{g}}$ are functions of the momentum space vectors $\mathbf{h}$ and $\mathbf{g}$, while $\Psi_n(\mathbf{R},\mathbf{g},z)$ is the $\mathbf{g}$th Fourier component of the channeling electron wave function at depth z calculated for the nth phonon configuration. The inelastic scattering coefficients $\mu_{\mathbf{h},\mathbf{g}}$ may be written as

$$\mu_{\mathbf{h},\mathbf{g}} = \frac{1}{2\pi k V_c}\sum_j \exp[-M_{\beta_j}(\mathbf{g}-\mathbf{h})]\exp[2\pi i(\mathbf{g}-\mathbf{h})\cdot \boldsymbol{\tau}_{\beta_j}] f_{\mathbf{h},\mathbf{g}}, \quad (2)$$

where $k \equiv |\mathbf{k}|$ is the magnitude of the wave vector of the incident electron and V_c is the volume of the unit cell. The sum occurs over all atoms of type β located at atom positions described by the vector $\boldsymbol{\tau}_{\beta_j}$ with Debye-Waller factors $M_{\beta_j}(\mathbf{g}-\mathbf{h})$. The inelastic atomic $f_{\mathbf{h},\mathbf{g}}$ scattering factors are given by

$$f_{\mathbf{h},\mathbf{g}} = \frac{1}{2\pi^3 a_0^2}\int k'\kappa^2 \left\{\int \left[\sum_{m_l} n_{m_l}\int F_{l,m_l}^{\beta *}(\mathbf{Q}_\mathbf{h},\boldsymbol{\kappa}) \times F_{l,m_l}^{\beta}(\mathbf{Q}_\mathbf{g},\boldsymbol{\kappa}) d\Omega_\kappa\right] \frac{d\Omega_{k'}}{|\mathbf{Q}_\mathbf{h}|^2|\mathbf{Q}_\mathbf{g}|^2}\right\} d\kappa. \quad (3)$$

The relativistic Bohr radius is denoted by a_0, k' is the magnitude of the wave vector $\mathbf{k}'$ of the inelastically scattered electron, and $\boldsymbol{\kappa}$ (magnitude κ) denotes the wave vector of the ejected electron. The quantum number associated with orbital angular momentum is denoted by l, with the azimuthal

 ©2007 The American Physical Society

quantum number m_l, with n_{m_l} electrons in each suborbital. For EELS, the integration over the solid angle $d\Omega_{k'} = \sin\theta d\theta d\phi$ is limited by the integration over θ to the range specified by the collection semiangle. This integration explicitly treats the scattered electrons as plane waves, which has been shown to be a reasonable approximation for other than small detectors.[13] However, we note that for thick specimens in STEM the validity of this approximation has not yet been fully explored, and will be the subject of further work. The range of integration over $\boldsymbol{\kappa}$ is determined by the energy window of interest. The atomic transition matrix elements F^{β}_{l,m_l} are functions of $\mathbf{Q_g}=\mathbf{q}+\mathbf{g}$, where $h\mathbf{q}=h(\mathbf{k}-\mathbf{k}')$ denotes the momentum transfer to the crystal. The atomic transition matrix element F^{β}_{l,m_l} for a specific suborbital labeled by the quantum numbers l and m_l is given by

$$F^{\beta}_{l,m_l}(\mathbf{Q_g},\boldsymbol{\kappa}) = \int b^{\beta *}(\boldsymbol{\kappa},\mathbf{r})\exp[2\pi i\mathbf{Q_g}\cdot\mathbf{r}]u^{\beta}_{l,m_l}(\mathbf{r})d\mathbf{r}. \quad (4)$$

Here, $u^{\beta}_{l,m_l}(\mathbf{r})$ and $b^{\beta}(\boldsymbol{\kappa},\mathbf{r})$ are the wave functions for the bound and continuum states, respectively.

The details of the core-loss transition are contained within the inelastic atomic form factors $f_{\mathbf{h},\mathbf{g}}$ which are the Fourier components of the inelastic atomic scattering potential. Because they are a function of two independent momentum space coordinates, $\mathbf{h}$ and $\mathbf{g}$, the resulting effective potential $W(\mathbf{r},\mathbf{r}')$ is nonlocal, i.e., a function of two independent real space coordinates $\mathbf{r}$ and $\mathbf{r}'$.[10] A common simplification is the so called local approximation where it is assumed $f_{\mathbf{h},\mathbf{g}} \approx f_{\mathbf{h}-\mathbf{g},\mathbf{0}} \equiv f_{\mathbf{f}}$, allowing the potential to be expressed in terms of a single real space coordinate. The importance of using a full nonlocal description of the effective ionization interaction has been demonstrated for conventional transmission electron microscopy,[14] and predicted for high resolution STEM images although yet to be demonstrated experimentally.[10]

It is important to distinguish between the terms "nonlocality" and "delocalization." The term nonlocality is used to describe the nature of the underlying inelastic potential.[15] The nonlocality arises because the inelastic atomic form factors $f_{\mathbf{h},\mathbf{g}}$ are functions of two independent Fourier space coordinates, $\mathbf{h}$ and $\mathbf{g}$, and therefore the potential itself is a function of two independent real space coordinates. This is closely related to the use of a mixed dynamic form factor.[16] Delocalization describes an extended spatial extent of the EELS signal, usually assumed to be a simple broadening. The delocalization of an image depends not only on the interaction leading to the energy loss but also on the elastic and other inelastic scattering of the probe, a complex combination of the inelastic scattering potential and the environment in which the scattering occurs. As shown below, atomic-resolution images cannot be interpreted using classical models based on impact parameters or simple estimates of image widths based on energy loss.[17]

III. EXPERIMENT

The sample for this study was a $LaMnO_3$ specimen prepared by conventional methods: grinding, dimpling, and Ar^+ ion milling. Final cleaning was done with 0.5 keV Ar^+ ions at an incident angle of 17°. This removes the thinnest areas, but also significantly decreases the amorphous layers on the specimen surface.[18] The thickness of the illuminated area was estimated to be approximately 250 Å. Electron microscopy observations were carried out in a dedicated scanning transmission electron microscope, a VG Microscopes HB501UX operated at 100 kV. This microscope is equipped with a Nion aberration corrector and a Gatan UHV Enfina electron energy loss spectrometer. Typical parameters for the aberration corrected VG HB501UX STEM are defocus $\Delta f = 62$ Å, third order spherical aberration coefficient $C_s = -0.05$ mm, and fifth order spherical aberration coefficient $C_5 = 63$ mm. A probe forming aperture of 20 mrad was used. Accounting for the electron source size of approximately 1.0 Å leads to a beam diameter of approximately 1.3 Å. Using a detector semiangle of 12 mrad, core-loss spectra were recorded as line scans along the ⟨110⟩ lattice direction. Following background subtraction, spectral images were then formed by integrating the EELS intensities over an energy window of 40 eV above the edge onset for the O K, La $N_{4,5}$, La $M_{4,5}$, and Mn $L_{2,3}$ absorption edges.

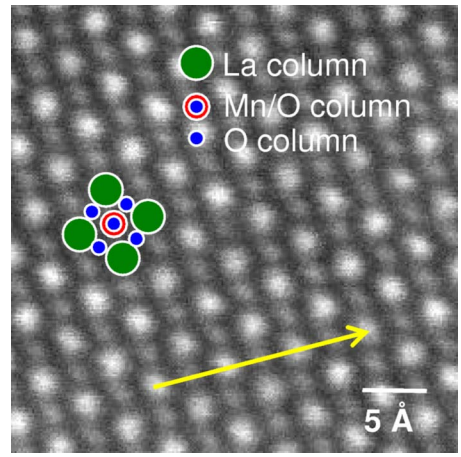

FIG. 1. (Color online) Annular dark field image of $LaMnO_3$ in the pseudocubic [001] zone axis orientation for a specimen approximately 250 Å thick. The ⟨110⟩ direction is indicated by the arrow.

IV. RESULTS AND DISCUSSION

An annular dark field (ADF) image of $LaMnO_3$ taken in the pseudocubic [001] zone axis orientation is shown in Fig. 1. The projected structure is indicated by the colored circles. The yellow arrow in Fig. 1 indicates the generic ⟨110⟩ lattice direction. Figures 2(a) and 2(b) show the measured zero-loss peak (ZLP) and ADF signals, respectively, along the ⟨110⟩ lattice direction (crosses) compared to simulation (solid line). In Figs. 2(c)–2(f), experimental integrated EELS line scans taken along the ⟨110⟩ lattice direction are compared with first principles nonlocal simulations using the experimental parameters listed in Sec. III. The higher energy edges have been aligned with the atomic columns using a simultaneous ADF line scan as a guide. Because of the lower energy of the La $N_{4,5}$ edge, its signal was acquired separately from a

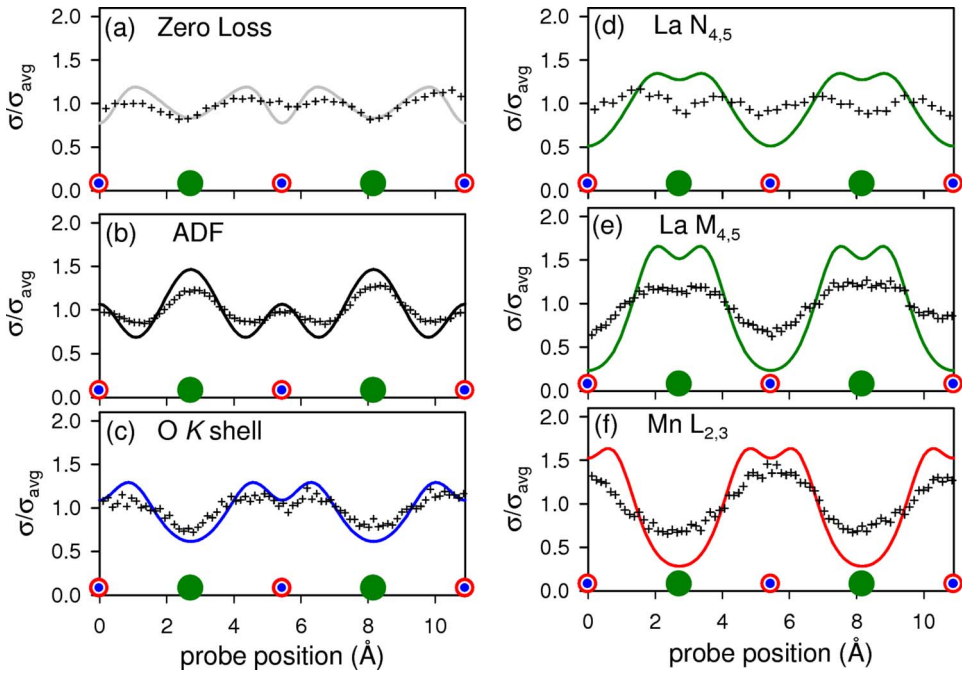

FIG. 2. (Color online) Experimental ⟨110⟩ line scans (crosses) and simulations (solid lines) for (a) the zero-loss peak, (b) annular dark field, (c) the O K edge, (d) the La $N_{4,5}$ edge, (e) the La $M_{4,5}$ edge, and (f) the Mn $L_{2,3}$ edge. The positions of the atomic columns are indicated by the filled circles.

section of the sample with similar thickness and the simultaneously acquired ZLP used as a guide for alignment. All simulations are calculated using a frozen phonon model.[19]

All simulated images have greater contrast variation than the experimental images. This is reminiscent of the so called Stobbs factor observed in high resolution transmission electron microscope intensity measurements.[20]

The ZLP signal shown in Fig. 2(a) exhibits a reduction of intensity above the atomic columns due to high angle scattering beyond the range of the EELS detector. The ADF signal shown in Fig. 2(b) has opposite contrast, exhibiting the usual approximately Z^2 variation of ADF images. Since electrons scattered through high angle to the ADF detector cannot also fall on the EELS detector, this reversal of contrast is to be expected.

Immediately striking is the shape of the images themselves. For the O K edge image shown in Fig. 2(c), there is an obvious dip or "volcano" located above the MnO columns. This is also clearly present in the La $N_{4,5}$ edge image shown in Fig. 2(d), with the other images in Figs. 2(e) and 2(f) showing a flattening of the peaks above the columns from which the signal originates. Such volcanolike structures have been noted previously in simulations[16,21] but have never been experimentally observed before. The O K and La $N_{4,5}$ edge images have similar contrast and width, despite significantly different binding energies. While it has been suggested that for the case of conventional transmission electron microscopy (CTEM), EELS signals should maintain the same contrast as the ZLP signal,[22] the difference in the shape and contrast of the La $M_{4,5}$ and $N_{4,5}$ suggests that the nature of the inelastic ionization potential is an essential part of inelastic image formation in STEM. It will be shown further below that the underlying physics leading to these structures is quite different for these different cases.

To understand why these effects are more pronounced for fine probes, Eq. (1) is rewritten for the case of an isolated atom whose thermal motion is ignored:

$$\sigma(\mathbf{R},t) \propto \sum_{\mathbf{h},\mathbf{g}} f_{\mathbf{h},\mathbf{g}} \Psi_{\mathbf{h}}^{*}(\mathbf{R}) \Psi_{\mathbf{g}}(\mathbf{R}) \Delta z, \tag{5}$$

where Δz is the thickness of the slice containing the atom. The range of the summation is restricted to nonzero values of $\Psi_{\mathbf{g}}$, determined by the probe forming aperture. In Fig. 3, $f_{\mathbf{h},\mathbf{g}}$ are plotted for parallel reciprocal space vectors $\mathbf{h}$ and $\mathbf{g}$ (for ease of display). The appearance of the form factor plots for the O K edge shown in Fig. 3(a) is similar to that of the La $M_{4,5}$ and Mn $L_{2,3}$ edge form factors shown in Figs. 3(c) and 3(d), respectively. For the La $N_{4,5}$ edge shown in Fig. 3(b), the structure of the plot is somewhat different, with the central peak being far narrower and a more complex distribution of negative form factors. In all cases, the aperture extends into the negative region of the form factor and the minimum value within the aperture is shown. The negative areas in the La $N_{4,5}$ edge plot cover a range of less than half that seen in the other plots. Similar behavior is found for the terms involving reciprocal vectors which are not parallel.

The contribution of negative values of the form factors to image formation is illustrated in Fig. 4, where images of isolated atoms have been simulated. This allows the examination of the nature of the ionization interaction without the complication of channeling. The projected electron density $\rho(\mathbf{r}_{\perp}) = \Sigma_{m_l} \int |u_{l,m_l}^{\beta}(\mathbf{r})|^2 \mathrm{d}z$ of the bound state from which the electron is ejected is shown by the solid background. The positive values of the form factors all produce "Gaussian-like" images peaked on the atomic site. The negative components produce a negative contribution to image formation

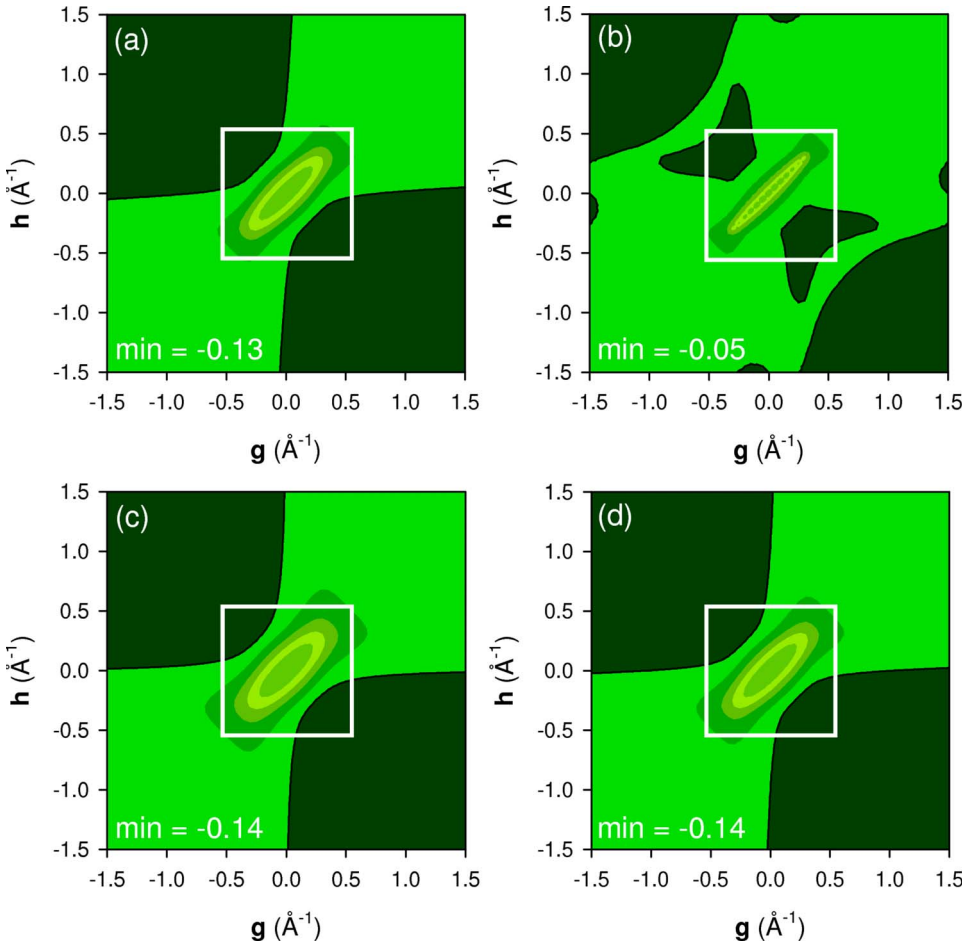

FIG. 3. (Color online) Inelastic atomic scattering form factors for parallel reciprocal space vectors for (a) the O K edge, (b) the La $N_{4,5}$, (c) the La $M_{4,5}$ edge, and (d) the Mn $L_{2,3}$ edge. The dark sections of the plots indicate negative values of $f_{\mathbf{h},\mathbf{g}}$ (Ref. 23). All form factors are normalized to have a maximum value of 1. The portion of the form factor included in the collection aperture is within the white squares in each case and the minimum value of $f_{\mathbf{h},\mathbf{g}}$ contained therein is indicated.

at the atomic site. Figure 4(a) shows that the O K edge image, whose form factor becomes the most negative, has a distinct dip at the atomic position. The form factors for the La $M_{4,5}$ and Mn $L_{2,3}$ edges are less negative and do not provide as large a modifying contribution at the atomic sites, and the La $M_{4,5}$ edge image shown in Fig. 4(c) has only a slightly flattened top. The magnitude of the negative components of the form factors included in the La $N_{4,5}$ image being smaller, it is peaked on the atomic site with a minimal negative component. As probe forming apertures can be made larger due to aberration correction and STEM probes become correspondingly smaller, the sum in Eq. (5) includes more negative components of the form factor and simulations show that volcanoes will be more pronounced, albeit narrower.[24]

An important consequence of the volcanoes is that the half-width at half maximum (HWHM) of the images is increased beyond that due to the positive form factor contributions. Thus, the HWHM of the La $N_{4,5}$ image is actually narrower than any of the other images despite having the lowest binding energy of 99 eV. This is contrary to classical estimates of the HWHM (see, for example, Ref. 17). However, the La $N_{4,5}$ image is still nonzero at a radius of 3 Å due to its long delocalized "tail."

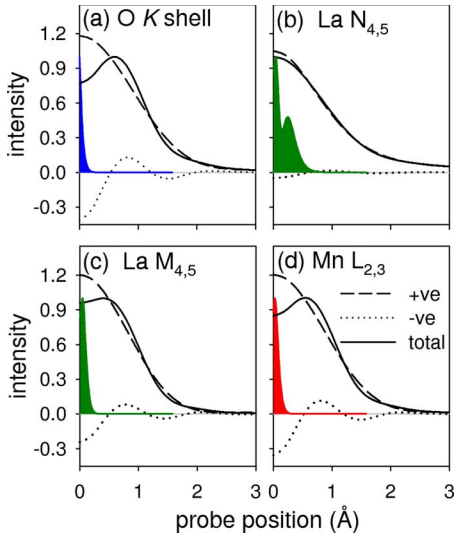

FIG. 4. (Color online) Single atom EELS images for (a) the O K edge, (b) the La $N_{4,5}$ edge, (c) the La $M_{4,5}$ edge and (d) the Mn $L_{2,3}$ edge. The contributions to the total intensity from positive and negative $f_{\mathbf{h},\mathbf{g}}$ are indicated by the dashed and dotted lines, respectively. The projected electron density of each bound state is shown by the solid background.

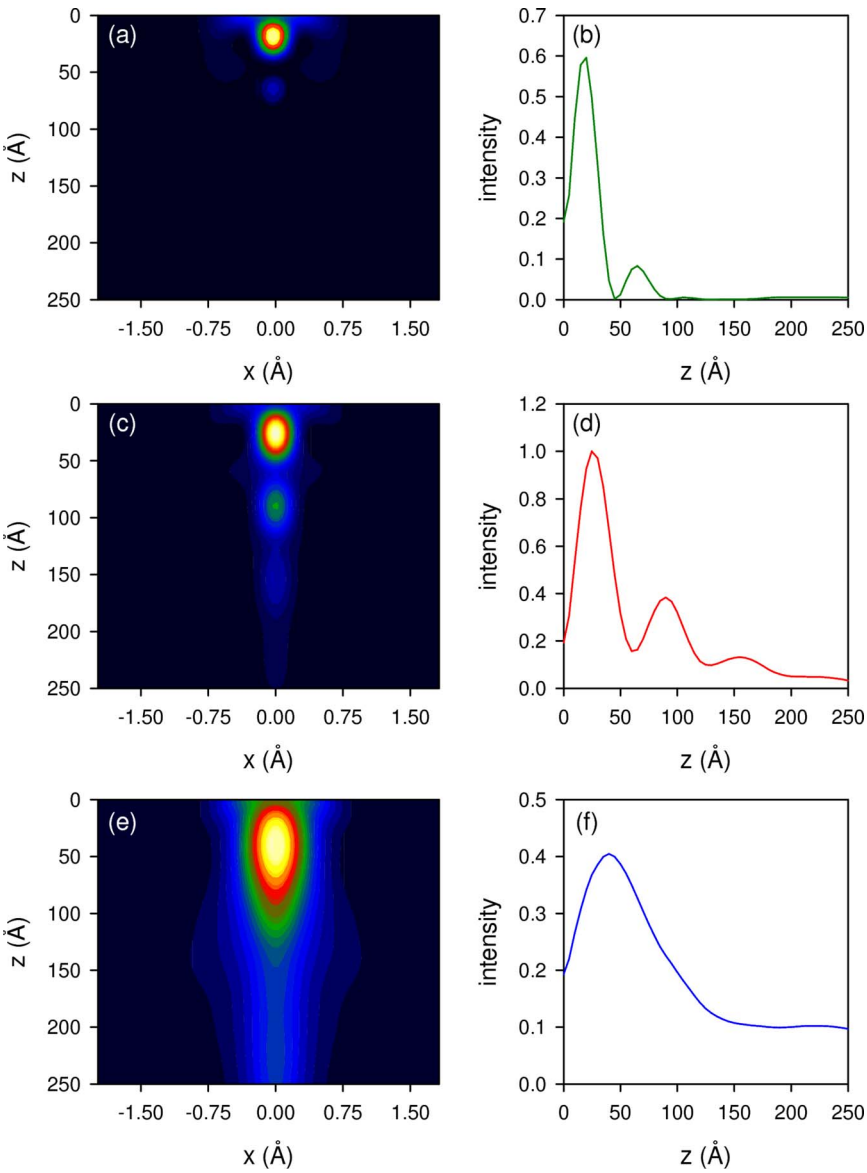

FIG. 5. (Color online) Probe intensity as a function of depth z for (a) the probe located above a La column with an intensity profile along the column shown in (b). Corresponding results for Mn/O columns are shown in (c) and (d), and O columns in (e) and (f).

The main difference between these single atom calculations is the bound state wave functions $u^{\beta}_{l,m_l}(\mathbf{r})$ used in calculating the transition matrix elements in Eq. (4). In Figs. 4(a), 4(c), and 4(d), the projected electron density of the bound states is peaked close to the atomic sites, far more so than the resulting single atom images. For La $N_{4,5}$ shown in Fig. 4(b), there is significant density away from the atomic site despite the fact that La $N_{4,5}$ yields the narrowest image. Clearly, there is no simple relationship between electron density of the initial state and image width, a consequence of subtleties of the underlying nonlocal nature of the interaction.[10]

Given the notably different atomic images for the O K and La $N_{4,5}$ edges, how can the similarity in shape and width of the line scans seen in Figs. 2(c) and 2(d) be explained? From Eq. (1), it is clear that the image depends not only on the inelastic scattering but also on the propagation or channeling of the incident electrons through the sample. The role of channeling of the STEM probe through a crystalline sample is most easily described for a probe at a fixed position $\mathbf{R}$.[25,26] In Fig. 5, the probe intensity is shown as a function of depth within the crystal for the probe placed over each of the atomic columns. When the probe is positioned above La columns [Fig. 5(a)], the intensity peaks at $z \approx 20$ Å with a small secondary peak at $z \approx 60$ Å. The intensity variation is seen more clearly in Fig. 5(b), where a line scan along the column is shown. Most of the intensity has dispersed by a depth of 100 Å and the La atoms are significantly illuminated for only the first 50 Å. When the probe is located above Mn/O columns [Figs. 5(c) and 5(d)], the probe has significant penetration for the first 100 Å and the intensity remains small but nonzero for the remaining depth of the crystal. For O columns [Figs. 5(c) and 5(d)], the intensity is significant for the entire crystal thickness, with the exit surface intensity being 50% of that at the entrance surface. Clearly, the channeling of the electron probe as it propagates through the sample plays an important role in image formation.

Figure 6 shows the evolution of the ZLP (left side) and ADF (right side) signals as a function of specimen thickness. For a single unit cell, the ZLP signal is essentially flat, with small reductions in intensity above the La and Mn/O col-

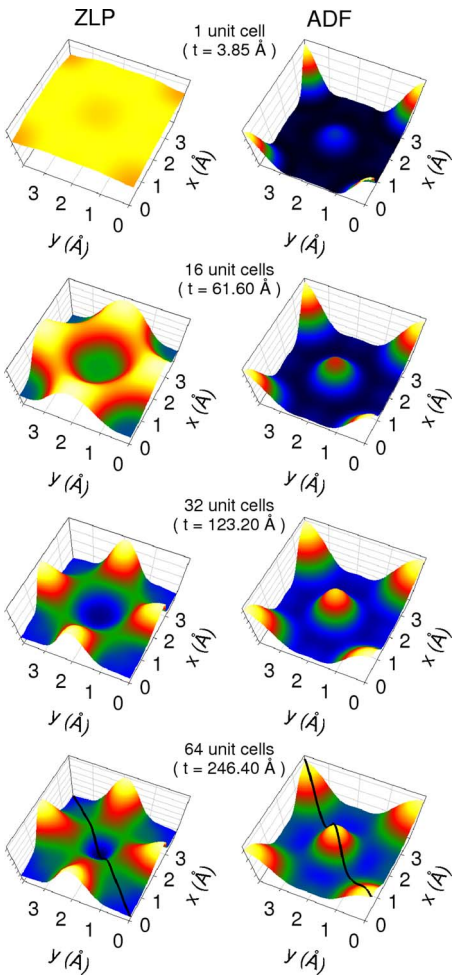

FIG. 6. (Color online) Zero-loss peak (ZLP) (left) and ADF (right) intensities as a function of specimen thickness. The black lines indicate the ⟨110⟩ scan direction.

umns. The ADF signal has maximum intensity above the La column with lesser intensity above the Mn/O column. Consistent with the results shown in Fig. 5, by a depth of 61.6 Å, there is a significant deficiency in the ZLP above the La columns and a correspondingly smaller volcano above the Mn/O column. Maximum intensity occurs on the O columns where the probe continues to have significant intensity as seen in Fig. 5(f). The peak above the Mn/O column in the ADF signal has increased slightly compared to that above the La columns, due to the higher incident electron density about this column at this depth. By the time the probe has channeled through 123.2 Å, there is only significant probe intensity remaining on the O columns. This is reflected in the ZLP signal, where the image is peaked above the O columns. The fact that the probe has significant intensity on the Mn/O column for approximately twice the depth that it has on the La column has led to an increase in the ADF signal above the Mn/O column relative to the signal above the La column. Since there is no further significant probe intensity on either the La or Mn/O columns after this depth, there is little change in the relative ADF signals for thicker samples.

In Fig. 7, the evolution of the images based on the measured edges as a function of crystal thickness across the whole unit cell is shown. The simulated images for a "crystal" one unit cell thick give the "atomic" images without the complication of channeling. The contribution to the image from each O column is identical at this stage. The O columns are only 1.93 Å apart and this results in considerable overlap between the images formed by each atomic column. (The blue circles represent the position where the volcanoes would occur if only individual atoms were considered.) This makes the interpretation of a single line scan difficult. As specimen thickness increases, the intensity above the central column in the unit cell shows a significant reduction. This column contains the heavier Mn atoms, which generate sig-

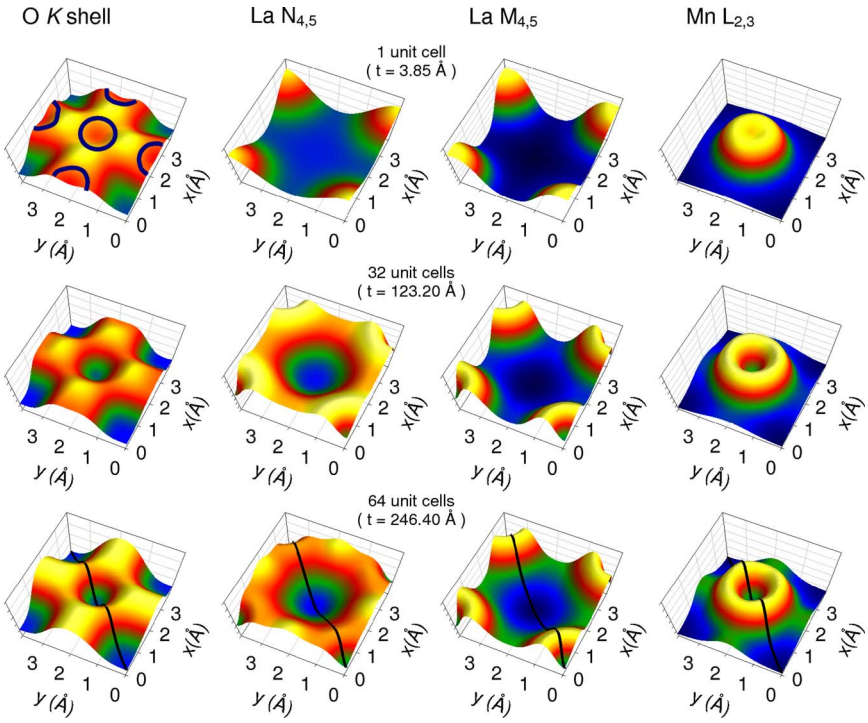

FIG. 7. (Color online) The evolution of spectroscopic images as a function of sample thickness for each of the measured EELS edges. These simulations do not include convolution with a source size term in order to emphasize the mechanisms underlying image formation. The black lines indicate the ⟨110⟩ scan direction.

nificant thermal diffuse scattering (TDS) and reduce the intensity on the column. By the time the sample is 64 unit cells thick, approximately the estimated thickness of the experimental specimen, this reduction in intensity has become substantial. A line scan taken in the ⟨010⟩ direction across alternating O/MnO/O columns would show a significant deficiency on the MnO column, possibly leading to the erroneous conclusion that there were fewer O atoms in the central column.

The La $N_{4,5}$ image for single unit cell thickness is more straightforward, with a peak on each atomic column. There is, however, considerable intensity away from the columns, with the minimum at the center of the unit cell being almost 40% of the on column intensity. As the sample becomes thicker, a volcano develops. With significant absorption due to TDS occurring when the probe is positioned above the La or MnO columns, there is less contribution to the image than when the probe is positioned above the O columns and interacting with the 40% "background." The small peaks above the O columns for 246.4 Å reflect the peaks in the ZLP seen in Fig. 5. This again leads to an image that is difficult to interpret without comparison to simulation. For the simulation at the greatest thickness, there are peaks on the O columns and relatively little intensity on the La columns.

It is interesting to compare the La $M_{4,5}$ edge image to that formed by the La $N_{4,5}$ edge. Because the signals originate from the same atoms, channeling and TDS are identical in both cases. The La $M_{4,5}$ image is, however, significantly localized about the La columns, with little overlap between columns even for the simulation for the greatest thickness shown here. The drastically different shape and distribution of these two cross sections illustrates clearly the importance of the inelastic scattering potential. While it has been shown that for CTEM low-loss EELS, "most inelastic scattering processes in crystals preserve image contrast to a first approximation,"[22] clearly for core-loss EELS, at least in the case of atomic-resolution STEM, this approximation is poor.

The image formed by the Mn $L_{2,3}$ edge is largely contained within the unit cell, consistent with previous results supporting column by column spectroscopy.[27] However, a significant deficiency in the edge intensity occurs above the column for increasing thickness due to TDS.

V. CONCLUSIONS

The interpretation of EELS line scans in the STEM based on core-loss spectroscopy requires an understanding of the subtle interplay between probe channeling or dechanneling and its effective nonlocal interaction with the atom being ionized. No simple connection exists between image width and either energy loss or the distribution of the electron density of the core state. Delocalization gives an extended tail to atomic images, which reduces contrast but does not preclude atomic resolution. In such cases, dechanneling from high-Z columns may lead to a volcanolike contrast at high thickness. Theoretical modeling is an essential adjunct to experiment, especially in the case where line scans, rather than a full two dimensional EELS map, are used. Without the understanding of image formation that simulation provides, there is a distinct possibility of erroneous interpretation of EELS data.

ACKNOWLEDGMENTS

This research was sponsored by the Office of Basic Energy Sciences, Division of Materials Sciences and Engineering, U.S. Department of Energy, under Contract No. DE-AC05-00OR22725 with Oak Ridge National Laboratory, managed and operated by UT-Battelle, LLC; and by the ORNL Laboratory Directed Research and Development Program. L.J.A. acknowledges the support of the Australian Research Council. K.v.B. acknowledges partial financial support from the Alexander von Humboldt Foundation. T.J.P. acknowledges support from the Microscopy Society of America.

[1] N. D. Browning, M. F. Chisholm, and S. J. Pennycook, Nature (London) **336**, 143 (1993); **444**, 235 (2006).
[2] D. A. Muller, Y. Tzou, R. Raj, and J. Silcox, Nature (London) **336**, 725 (1993).
[3] P. E. Batson, Nature (London) **336**, 727 (1993).
[4] P. E. Batson, N. Delby, and O. L. Krivanek, Nature (London) **418**, 617 (2002).
[5] P. D. Nellist, M. F. Chisholm, N. Dellby, O. L. Krivanek, M. F. Murfitt, Z. S. Szilagyi, A. R. Lupini, A. Borisevich, W. H. Sides, Jr., and S. J. Pennycook, Science **305**, 1741 (2004).
[6] L. J. Allen and T. W. Josefsson, Phys. Rev. B **52**, 3184 (1995).
[7] M. P. Oxley and L. J. Allen, Phys. Rev. B **57**, 3273 (1998).
[8] L. J. Allen, S. D. Findlay, M. P. Oxley, and C. J. Rossouw, Ultramicroscopy **96**, 47 (2003).
[9] S. D. Findlay, M. P. Oxley, S. J. Pennycook, and L. J. Allen, Ultramicroscopy **104**, 126 (2005).
[10] M. P. Oxley, E. C. Cosgriff, and L. J. Allen, Phys. Rev. Lett. **94**, 203906 (2005).
[11] H. Rose, Optik (Jena) **45**, 139 (1976).
[12] D. A. Muller, B. Edwards, E. J. Kirkland, and J. Silcox, Ultramicroscopy **86**, 371 (2001).
[13] T. W. Josefsson and L. J. Allen, Phys. Rev. B **53**, 2277 (1996).
[14] L. J. Allen, S. D. Findlay, M. P. Oxley, C. Witte, and N. J. Zaluzec, Ultramicroscopy **106**, 1001 (2006).
[15] P. H. Dederichs, *Solid State Physics: Advances in Research Applications* (Academic, New York, 1982), pp. 136–229.
[16] H. Kohl and H. Rose, Adv. Electron. Electron Phys. **65**, 173 (1985).
[17] R. F. Egerton, *Electron Energy-Loss Spectroscopy in the Electron Microscope*, 2nd ed. (Plenum, New York, 1996).
[18] A. Strecker, U. Bäder, M. Kelsch, U. Salzberger, M. Sycha, M. Gao, G. Richter, and K. van Benthem, Z. Metallkd. **94**, 290 (2003).
[19] E. J. Kirkland, *Advanced Computing in Electron Microscopy* (Plenum, New York, 1998).
[20] M. J. Hÿtch and W. M. Stobbs, Ultramicroscopy **53**, 191 (1994).

[21] E. C. Cosgriff, M. P. Oxley, L. J. Allen, and S. J. Pennycook, Ultramicroscopy **102**, 317 (2005).
[22] S. L. Cundy, A. Howie, and U. Valdrè, Philos. Mag. **20**, 147 (1969).
[23] M. P. Oxley and L. J. Allen, Acta Crystallogr., Sect. A: Found. Crystallogr. **57**, 713 (2001).
[24] M. P. Oxley, M. Varela, K. van Benthem, and S. J. Pennycook, in *Proceedings of the International Conference on Density Functional Theory and Transmission Electron Microscopy*, edited by J. Luitz, C. Hérbert, K. Weinmeier, P. Blaha, C. Ambrosch-Draxl, and P. Schattschneider (Physicae et chimicae solidorum amici, Vienna, Austria, 2006), p. 22.
[25] J. Fertig and H. Rose, Optik (Jena) **59**, 407 (1981).
[26] C. Dywer and J. Etheridge, Ultramicroscopy **96**, 343 (2003).
[27] L. J. Allen, S. D. Findlay, A. R. Lupini, M. P. Oxley, and S. J. Pennycook, Phys. Rev. Lett. **91**, 105503 (2003).